Effect of the Ionic Strength and pH on the Equilibrium Structure of a Neurofilament Brush

E. B. Zhulina* and F. A. M. Leermakers[†]

*Institute of Macromolecular Compounds of the Russian Academy of Sciences, St. Petersburg, Russia; and [†]Laboratory of Physical Chemistry and Colloid Science, Wageningen University, Wageningen, The Netherlands

ABSTRACT   Using the numerical model of Scheutjens and Fleer, we investigated, on a self-consistent field level, the equilibrium structure of the neurofilament brush formed by projection domains of the constituent NF-H, NF-M, and NF-L proteins. The phosphorylation of such a brush is a major regulatory process that triggers the relocation of the H tails from the NF core to the brush periphery. We explore how the pH and the ionic strength affect the rearrangements in the NF brush structure upon phosphorylation. We demonstrate that the translocation of H tails in an individual NF occurs as a sharp cooperative transition below and up to the physiological salt concentration. Regularities of this process are reminiscent of the collapse-to-stretching transition in a cylindrical polyelectrolyte brush in a poor solvent. The effect of pH at physiological ionic strength is noticeable only in the acidic range and is more pronounced for a dephosphorylated NF.

INTRODUCTION

In neuron physiology, there is a large effort to relate the spatial distribution of intermediate filaments in axons and dendrites to human neurodegenerative diseases (1). Neurofilament proteins are major constituents of the cellular cytoskeleton in neurites. They mediate the axonal caliber and participate in various regulatory processes (2–4). The abnormal accumulation and aggregation of neurofilaments (NFs) is linked to the development of amyotrophic lateral sclerosis, Lewy-body-type dementia and Parkinson disease (1,2). At present, the ultrastructural organization of neurofilaments, its evolution in the process of axonal growth and maturation, and the possible association of the NFs with other neuronal intermediate filament proteins are not fully understood (5,6).

It is known that NFs are composed of three distinct proteins labeled as NF-L (light), NF-M (medium), and NF-H (heavy) according to their molecular weights (5). Each one of these proteins contains a rigid domain of ∼310 amino-acid (aa) residues close to the N-terminus and a so-called projection domain (nonstructured flexible tail) at the C-terminus. In human NFs the numbers of aa residues are $N_H = 607$, $N_M = 504$, and $N_L = 142$ for the NF-H, NF-M, and NF-L projection domains, respectively (Human Intermediate Filament Database, http://www.interfil.org/proteins.php). The backbone of a mature NF consists of four protofilaments and has a radius R of ∼5 nm (7,8). It comprises the rigid domains of the triplet proteins and has a persistence length of ∼100 nm. In human adult NF, the stoichiometric ratio of L/M/H proteins is 7:3:2 (5), yielding on average distances of ∼2.5, 5.5, and 8.5 nm between tails L, M, and H, respectively. This relatively dense emanation of the flexible unstructured side arms from the NF core inspired a polymer brush view of the projection domains (9,10). In this framework, one considers the projection domains of the three constituent proteins being homogeneously end-grafted onto a rigid impenetrable cylinder (the NF backbone). The polymer brush model of NF side arms (Fig. 1) provides a useful framework to rationalize the experimental findings for neurofilaments both in vitro and in vivo (10–13). It also suggests a mechanism for the mechanical protection of axons and dendrites (9).

In a polymer brush, the chain conformations are strongly affected by the intermolecular interactions, especially when the polymers comprise charged groups. In the case of the triplet NF proteins, the H, M, and L tails are strongly ionized at physiological pH ≈ 7. Each of them contains various positively- and negatively-charged aa residues. The M and L tails appear to be overall negatively-charged polyelectrolytes, whereas the H tail is almost a net neutral polyampholyte (with just one excess negative charge). The phosphorylation of the side arms that results from the uptake of some additional negative charge by the H and M tails increases the electrostatic interactions between the tails and triggers a major transformation of the NF brush structure.

In our previous study (14), we applied the Scheutjens-Fleer self-consistent field (SCF) method to probe theoretically the organization of a human NF accounting for different length and composition of the triplet NF-H, NF-M, and NF-L proteins. The numerical SCF technique is widely used in polymer science and it was successfully applied previously to investigate the behavior of multicomponent species in solutions and at interfaces (15–17). In the case of a neurofilament, the cylindrical geometry was implemented. Here, the conformationally ordered parts of the triplet proteins (coiled-coil domains) were represented by a rigid cylinder onto which the flexible tails of the three different types (H, M, and L), with their specified amino-acid sequences, were grafted.
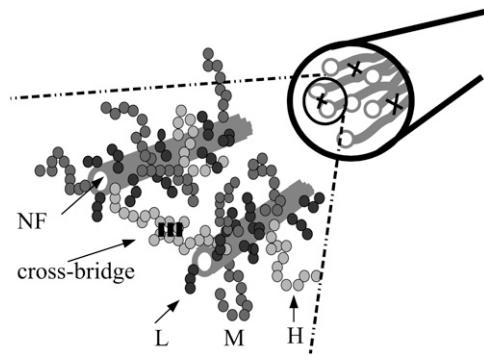
FIGURE 1 Schematic illustration of the neurofilament cytoskeleton. On the right, a simple view of the large scale structure is given (illustrating the NF only), where the crosses represent cross bridges and the shaded lines the NFs. On the left two fragments of the NFs are shown with a rigid backbone (in *shading*) with three types of projection domains. The black short ones are the NF-L chains, the longer ones (in *medium shading*) are the NF-M and the longest ones (*lightest shading*) represent the NF-H chains (with number ratio 7:3:2). The latter ones can form cross bridges with their terminal KEP repeats. We speculate that they do this frequently when the serines in the KEP domains are phosphorylated. Note that in the calculations there is one coarse-grained segment for each aa residue. In this article, we consider an isolated NF brush only.

We explored the internal structure of the NF brush, taking the hydrophobicity and the state of ionization of each aa residue as realistic, as possible into account. We anticipated that, due to the relatively dense tethering of the tails, the possible gradients in the lateral direction could, in first-order, be ignored. This allowed us to implement the one-dimensional version of the SCF model, which permitted the evaluation of the polymer density gradients in the direction normal to the backbone.

The one-dimensional SCF modeling revealed various distinct features of the NF brush organization. It demonstrated that a moderate enzymatic phosphorylation of the side arms (involving the serines in the KSP repeats only) leads to a major rearrangement of the NF brush structure. Under the conditions of physiological pH $\approx$ 7 and at relatively low ionic strength of 0.01 M of a 1:1 salt, a dephosphorylated NF exhibits a clear separation of the H, M, and L tails in the direction normal to the filament backbone. Namely, the longest tails (H) concentrate near (envelop) the NF core, the shortest tails (L) occupy the proximal (intermediate) part of the NF brush, and the M tails are expelled to the brush periphery, picking up flowerlike conformations. The terminal KEP domains of the H tails (responsible for cross-bridging with other filaments (18,19)) are thus localized near the backbone in a dephosphorylated neurofilament. The phosphorylation of the serines in the KSP repeats transforms the polyampholytic H tail into a negatively charged polyelectrolyte. As a result, the mutual repulsion of similarly (negatively) charged tails (H, M, and L) leads to the expulsion of the H tails to the periphery of the NF brush. Due to the increase in electrostatic interactions, the total brush

thickness increases. Similarly to the M tail, the longest tail (H) acquires a flowerlike conformation (the almost uniformly stretched stem is crowned by a coiled terminal KEP domain, now relocated to the NF brush periphery). This transition occurs when nearly half of the KSP repeats in the H tails is phosphorylated. Based on the predicted translocation of the KEP domain, we speculated that at moderate phosphorylation, in addition to the increase of the NF brush thickness, the propensity of H tails to cross bridge also enhances.

At this stage it is clear that the SCF modeling allowed us to discuss trends in the response of the NF brush to the enzymatic phosphorylation of the side arms. It is also possible to evaluate the response of the NF structure to the relevant physical/chemical parameters. Indeed, the intraaxonal pH and salinity is subject to change as it may, for example, vary under pathological conditions. The goal of this article is therefore to explore systematically how variations in the ionic strength and in the solution pH affect the phosphorylation-induced rearrangement of the NF brush structure. We will demonstrate that 1), the qualitative picture of the NF brush transformation (as formulated in our previous article (14)) remains valid up to relatively high ionic strength (up to and slightly beyond in vivo values); 2), the relocation of the KEP domains to the periphery of the NF brush is a cooperative transition that occurs when almost half of the KSP repeats in the H tails are phosphorylated (even at low ionic strength); and 3), the specific features of this relocation (the transition point, the pre- and post-transition states) can be rationalized within an analytical framework for the collapse-to-stretching transition in a polyelectrolyte cylindrical brush.

The remainder of this article is organized as follows. In Model and Method, we briefly review the model and the SCF technique that were used in our previous work. The novel results of the SCF modeling are presented in Results and Discussion. We discuss and compare these results with the predictions of our analytical approach. The analytical model for a cylindrical polyelectrolyte brush is presented in the Appendix. Finally, we summarize our results and conclusions.

MODEL AND METHOD

The application of the Scheutjens-Fleer SCF technique requires coarse-graining of the NF tails. Modeling of the side arms of the triplet of NF proteins is performed with two distinct levels of coarse-graining. First, each aa residue is modeled as a symmetric cubic monomer with bond length $a = 0.6$ nm. Subsequently, a copolymer-type or fine-type coarse-graining is applied.

In our first, copolymer-type model c, the L, M, and H tails are envisioned as a neutral/anionic block copolymer, an anionic homopolymer, and an anionic/cationic block copolymer, respectively. The numbers of monomers in respective blocks are chosen to capture the general trends in the charge distribution along the tails (see Fig. 2 and (14)). The solubility parameters of all aa residues are assumed to be the same: the Flory interaction parameter that determines the free energy difference between monomer-water and monomer-monomer and water-water contacts is set to $\chi = 0.6$ (this

H   100(−0.230)   507(+0.043)

M   504(−0.103)

L   50(0)   92(−0.252)

FIGURE 2 The NF-L, NF-M, and NF-H projection domains envisioned as block copolymers in model c. The first number above each block indicates the number of aa residues, the number in brackets is the partial charge, in units of the elementary charge, per residue.

parameter is, as usual, made dimensionless by the thermal energy k_BT). This value of χ corresponds to moderately poor solvent conditions for these aa residues (the monomers are weakly attracted to each other). All other interaction parameters for aa-backbone, aa-ion, ion-ion interactions, etc., are assumed to be zero.

In our second, fine model f, the actual distribution of the charged monomers and the different hydrophilicities of the aa residues are conserved in each of the tails. The set of aa residues is divided into five groups: the apolar residues $\mathbf{A} \in \{G, P, C, M, A, L, V, I\}$, the polar residues $\mathbf{N} \in \{Y, Q, N, H, F, W, T, S'\}$, the charged ones $\mathbf{P} \in \{K, R\}$ and $\mathbf{M} \in \{E, D\}$, and the chargeable (i.e., subject to phosphorylation) units $\mathbf{C} \in \{S\}_{KSP}$. Here, the serines S in the KSP repeats and the serines S' located elsewhere are placed in separate groups. The coarse-grained aa sequences in the H, M, and L tails are presented in Table 1. The digit to the right of each group label ($\mathbf{A, N, P, M}$, or $\mathbf{C}$) indicates the number of repeating aa residues of the specified type, and the brackets are used when there is a sequence of repeating aa residues. Unified dissociation constants $K_a = 5$ and $K_b = 5$ are assigned to acidic ($\mathbf{M}$) and basic ($\mathbf{P}$) aa residues. Different solubilities (values of the Flory χ-parameter) and dielectric constants ϵ are introduced for apolar, polar and charged aa residues (see (14)). The coarse-grained tails are tethered to the cylindrical core of the NF with the appropriate stoichiometry (7:3:2), and the value of $R = 8a$ (corresponding approximately to $R = 5$ nm) for the core radius is used in all the SCF calculations.

We account for a moderate enzymatic phosphorylation of the H and M tails that involves the KSP repeats only and introduce an effective valence v_c

for a serine in a KSP repeat, which changes from 0 to -2 upon the uptake of negative charges due to phosphorylation. The total charge ΔQ acquired by a tail is then expressed as $\Delta Q = v_c N_{KSP}$ where N_{KSP} is the total number of KSP repeats in the tail. A value of $v_c = -1$ corresponds to the state in which 50% of all KSP repeats are phosphorylated.

As in our previous study we use the one-dimensional version of the SCF model. In this framework, the spatial distributions of all the components ($\mathbf{A}$, $\mathbf{N}$, $\mathbf{P}$, $\mathbf{M}$, $\mathbf{C}$, ions, water) depend exclusively on the distance z from the NF backbone and are smeared in lateral direction (i.e., along the NF backbone). The goal of the SCF calculation is to find the equilibrium distance-dependent distributions of all the species in the system including the components $X = \mathbf{A, N, P, M}$ or $\mathbf{C}$ of the H, M, and L tails, water, added ions, etc., collected in the volume fraction $\varphi_X(z)$ profiles. The search for these equilibrium distributions implies the introduction of effective potential fields $u_X(z)$ (for each monomer type X in the system). All possible and allowed chain conformations are generated in a freely-jointed chain model, wherein the statistical weight of each conformation thus depends on the potentials felt by its segments. After normalization of these statistical weights to the grafting density, the current distribution of all the species is determined. As usual, the current distribution of the polymer and all ions $\varphi_X(z)$ specifies the potentials acting on all the components. Part of the segment potential is the electrostatic contribution. For this the full (i.e., nonlinearized) Poisson-Boltzmann equation is solved. Another part of the segment potential is linked to the incompressibility constraint $\sum_X \varphi_X(z) = 1$, which is obeyed in each coordinate z. The short-range interactions (with the strength given by the χ-parameters) are accounted for in the Bragg-Williams approximation. The numerical procedure that solves the equations is finished when the potential fields become self-consistent, that is that the potentials both determine and follow from a fixed set of volume fractions. More details can be found in our previous publication (14) and the basic literature on the SCF modeling (see (20) and references therein).

RESULTS AND DISCUSSION

Dephosphorylated individual NF

We start with analyzing polymer volume fraction profiles $\varphi(z)$ for the H, M, and L tails in an individual dephosphorylated NF in solution for a given pH $= 7$ and variable ionic strength.

TABLE 1 1 Coarse-grained projection domains in model f

The H-chain:
NA$_4$N$_2$A$_2$ MA$_3$PA$_2$ NAN$_3$(AP)$_2$N M$_2$(PA)$_2$AM PNMP MNA$_3$(M$_2$N$_2$)$_2$ (ANM$_2$)$_2$M$_2$PM (APM$_3$)$_2$A$_2$M$_4$A MA$_2$M$_3$N PCA$_3$M$_2$ A$_2$NAM PMAP CA$_2$PM$_2$ APCA$_2$ MAPC AMPM$_2$ APCA$_2$ MAPC AMPA PCA$_2$P M$_2$APC A$_2$MAP CAMP M$_2$APC A$_2$MAP CAMP APCA$_2$ PM$_2$ AP CA$_2$MA PCAM PAPC A$_2$PM$_2$A PCA$_2$M APCA$_2$ PM$_2$AP CA$_2$MA PCAM PAPC ANPM$_2$ APCA MPAP CAMP M$_2$APC AMPA PCA$_2$P AMAP CAMP APCA$_2$ PAMA PCAM PAPC A$_2$PM$_2$A PCAM PAPC A$_2$PM$_2$A PCAM PAPC A$_2$PM$_2$A PNAM PAPC A$_2$PM$_2$A P(CAMPAP)$_2$NA MAPC AMAP NA$_2$PM$_2$ APNA$_2$ MPNA MPA PCA$_2$P M$_2$APC AMPA PCA$_2$P M$_2$APA$_2$ MPMA$_2$ P$_2$M$_2$AP CA$_2$PM$_3$PA-*NM(AP)$_2$MA$_2$ P$_2$AM$_3$P A$_3$NAP NM$_2$P$_2$M NP$_2$M$_2$A$_2$ P$_2$MA$_2$(PA)$_2$ M$_2$P$_2$MA$_3$ MPAP MNPA MAP$_2$M$_2$ AM$_2$P$_3$A$_2$ NAMP MA$_3$PA MAPM$_2$ (AP)$_2$MPN MA$_2$P$_2$M AM$_2$(AP)$_2$M ANPA$_2$M P$_2$MA$_3$M P$_2$MNP M$_2$PAP$_2$ AM$_2$PA PNM(AP)$_2$ M$_3$PNA NPMA N(PA)$_2$MP AMPN$_4$(MNP)$_2$ A$_2$MPA NM$_2$PA (AP)$_2$*

The M-chain:
N$_3$A$_2$(NA)$_2$A$_2$ N$_3$PA$_3$N AN$_2$PA NPNP AMA$_2$(PA)$_2$ N$_2$PNA M$_2$A$_2$M$_2$N PAM$_3$P NMAM$_2$ (A$_2$N)$_2$M$_2$A$_3$N APM$_2$P$_2$ MA$_2$M$_2$P M$_3$(AM)$_2$M$_3$A$_3$ P$_2$CA$_2$P ANA$_2$MA PM$_3$AM PM$_4$AN M$_8$A$_2$P NMNA M$_2$A$_2$NM PMAN$_2$ MPM$_2$A MNM$_2$A MNM(AM)$_3$ (MA)$_2$PM$_2$P$_2$ AM$_2$PN M$_2$A$_2$NP M$_2$A$_3$MA PAMP AMPA PCA$_3$P CA$_2$M$_2$P APCA$_3$ PCA$_2$M$_2$ PAPC A$_3$PCA$_2$ M$_2$PAP CA$_3$PC A$_2$M$_2$PA PCA$_2$NPCA$_2$M$_2$ PAPC A$_3$PCA$_2$ M$_2$APN PAMA$_2$ PAMN PM$_3$PM APMA$_2$ PM$_2$PA MP$_2$M$_2$P APMA$_2$ MP$_3$AM NA$_2$PM$_2$ A$_3$MA$_2$N ANPN APAN AMPM NPM$_2$A PA$_2$N$_2$(MP)$_3$ A$_3$MA$_2$N M$_3$ANM PA$_2$PA NP$_2$M$_2$A$_3$ N(AM)$_2$AP M$_2$A(MN)$_2$P MPAN APM$_3$P A$_3$N$_2$A$_2$M ANA$_2$M$_2$P$_2$A$_2$MP NM$_2$PA$_3$ NPNA MPAN$_2$ (MA$_2$)$_2$(NPNA)$_2$NA N$_2$PA(M$_2$N)$_2$ NM$_2$PA$_2$ N$_2$P$_2$AM PAN$_3$A$_3$ PMAN$_3$M

The L-chain:
N$_3$A$_2$(NAN)$_2$N$_4$ (NA)$_2$P(NA)$_2$A$_2$ N$_5$A$_2$N$_2$P N$_2$AN$_6$A NM$_2$N$_2$M AM$_2$NA MANP AM$_2$AP M$_2$A$_2$N(MA)$_2$ M$_4$(PM)$_2$M(AM$_4$A)$_2$M$_4$A PM$_2$NM$_2$ APM$_4$A$_2$ M(AM$_2$)$_2$NP MAM$_4$P$_2$ AMA$_3$M$_2$ NA$_2$P$_3$M

A number behind the segment name (or sequence) indicates the length of this repeat. The following amino-acid assignments were made: $\mathbf{A} \in \{G, P, C, M, A, L, V, I\}$, $\mathbf{N} \in \{Y, Q, H, F, W, T, S'\}$, $\mathbf{P} \in \{K, R\}$, $\mathbf{M} \in \{E, D\}$, $\mathbf{C} \in \{S\}_{KSP}$. The terminal KEP-segment of the H chain is in italics.

In Fig. 3, we present a selection of the volume fraction profiles for the three projection domains as a function of the distance z from the backbone for three different values of salt concentration $c_s = 0.01$ M (a), 0.1 M (b), and 1 M (c). All the data in Fig. 3, a–c, correspond to model f with the fine coarse-graining of the side arms. The data of Fig. 3 a were already discussed in our previous article (Fig. 3 a in (14)), and are reproduced here for convenience. Also for comparison, in Fig. 3 d we plotted the polymer density profiles for model c (copolymer type of coarse graining) at $c_s = 1$ M. For this highest solution salinity the maximal differences between the two models, f and c, are anticipated.

The increase in the ionic strength of the solution leads to an overall contraction of the NF brush and a redistribution of the side arms. A comparison of Fig. 3 a ($c_s = 0.01$ M) and 3 b ($c_s = 0.1$ M) indicates that the general structural organization of the NF brush is retained up to values of the physiological ionic strength. Namely, the long (H) tails remain concentrated near the backbone, the intermediate (M) tails are found on the outside at the brush periphery, and the shortest (L) tails still reach the proximal part of the brush. The polymer density profile for the H tails is virtually unaffected by this 10-fold increase in the solution salinity. However, for both M and L tails, the volume fraction increases near the backbone due to the diminished extension of these tails. The cutoff point for the corresponding volume fraction profiles shifts from $z/a \approx 70$ to ≈ 50 for the M tails and from $z/a \approx 40$ to ≈ 30 for the L tails.

A further 10-fold increase in the ionic strength ($c_s = 1$ M, Fig. 3 c) leads to a considerable reorganization of the NF brush. Now the electrostatic interactions are strongly screened by salt ions, and the brush behavior is largely dictated by the nonelectrostatic interactions. The tails (H, M, and L) exhibit almost similar polymer volume fraction profiles. Close inspection shows, however, that the H tails now protrude more

to the brush periphery, and their volume fraction near the backbone decreases. This is correlated with a noticeable increase in the volume fraction of the M tails near the NF backbone.

Fig. 3 d presents the polymer volume fraction profiles for the coarse-grained tails in model c. In the framework of this model, the M and H tails are much more extended (the cutoff for these volume fraction profiles is at $z/a \approx 40$). One should keep in mind, however, that the solubility parameter is fixed to $\chi = 0.6$ for all aa residues and that model c corresponds effectively to somewhat weaker attraction between monomers than in the fine model f. More specifically, the chosen value of the Flory parameter $\chi = 2$ for **A** monomers (apolar aa residues that constitute $\sim 30\%$ of all aa residues in the H and M tails) insures a higher average hydrophobicity of these tails in model f. The differences in the solubility parameters for the aa residues are less significant for the two models when the electrostatic interactions dominate (i.e., at low ionic strength $c_s = 0.01$ M, see (14)). The assigned values of the Flory parameter become more important at high solution salinity ($c_s = 1$ M). An increase in χ from $\chi = 0.6$ to $\chi = 0.8$ in model c makes the polymer density profiles for all the H, M, and L tails in Fig. 3 d closer to those in Fig. 3 c (not shown).

The distribution of the free ends of the projection domains contains additional information on the chain conformations. In Fig. 4 we show the end-point distributions $g(z)$ of the terminal monomers (chain ends) that correspond to the overall volume fraction profiles of the projection domains presented in Fig. 3. Within the fine model there is a number of significant observations that present themselves as a function of the ionic strength. The end-point of the smallest (L) projection domain is positioned in two populations at low ionic strength condition, which is seen by the shoulder at $\sim z/a \approx 25$ (Fig. 3 a). This shoulder merges with the main distribution
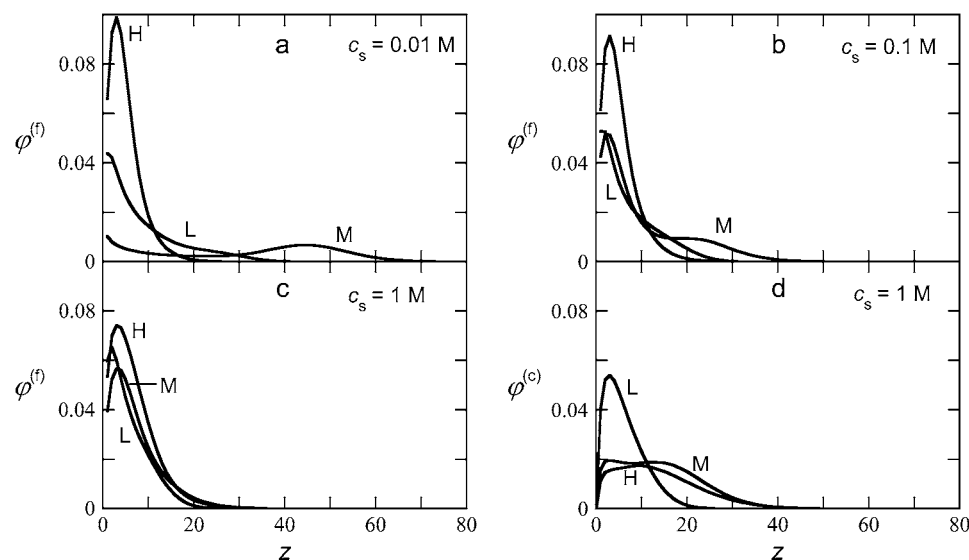
FIGURE 3 The volume fraction profiles of the high (H), medium (M), and low (L) projection domains of the NF brush at pH $= 7$. For the fine model: (a) $c_s = 0.01$ M, (b) $c_s = 0.1$ M, and (c) $c_s = 1$ M; and the copolymer model (d) $c_s = 1$ M.
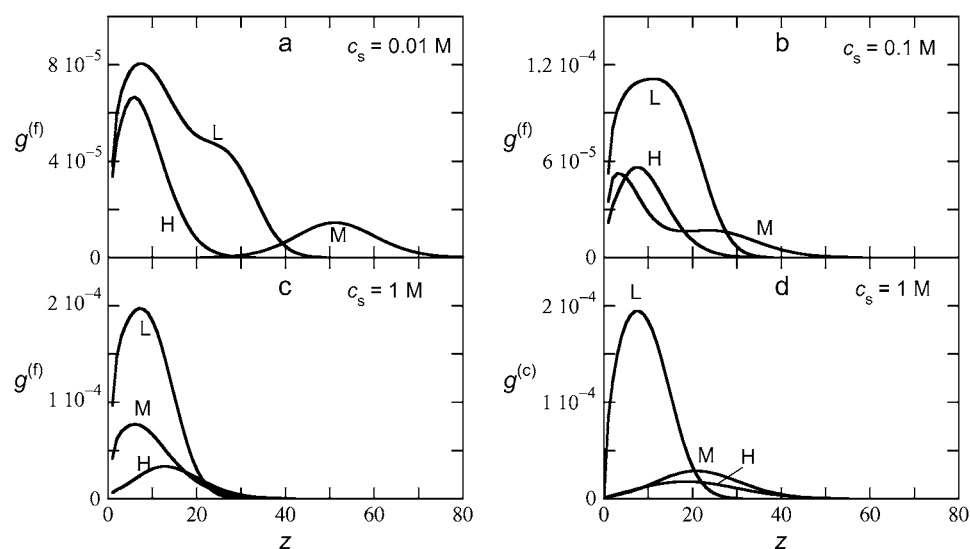
FIGURE 4 The end-point distributions ($g(z)$) corresponding to the overall volume fraction profiles given in Fig. 3.

when the ionic strength is $c_s = 0.1$ M, and the single population of chains retracts toward the core with a further increase of the ionic strength (Fig. 3 b). The M chain has its ends exclusively at the periphery at low salt strength, and the end distribution becomes bimodal at intermediate ionic strength (Fig. 3, a and b). The end-point distributions of all the tails become similar at high ionic strength (Fig. 3 c). The long chain (H) has an unimolar distribution for all ionic strengths (Fig. 3, a–c), and the chain end moves gradually to higher z-value with increasing ionic strength. In the copolymer model (Fig. 4 d), the chain ends resemble those of the corresponding (f) result (Fig. 4 c), albeit that the ends are overall positioned at higher z-values. This effect was already explained above, where we argued that this is because in model c the chains are modeled as being in a slightly less unfavorable solvent than in model f.

At physiological ionic strength ($c_s \approx 0.15$ M), there is significant screening of the charges in the projection domains. Under these conditions, it is expected that the pH is still affecting the structure of the NF brush. Fig. 5 demonstrates the distributions (polymer volume fraction profiles) of the side arms for three pH values, or well below, near (pH = 7), and well above physiological conditions. From these results we conclude that the NF structure becomes almost independent of the pH above pH = 7, whereas significant changes are expected at acidic situations. The M tail, especially, becomes less extended at these conditions. The relative weak dependence on the pH is caused by the fact that the acidic and basic aa groups have titrated each other to a large extent. A change in pH around the physiological relevant value does not change this greatly. Only at the extreme scale of the pH the major changes are found (not shown).

Phosphorylated individual NF

We now consider the phosphorylation of an individual NF brush under the conditions of physiological pH = 7 and

focus on the effects of the ionic strength. In our previous article (14) we demonstrated that at relatively low ionic strength, $c_s = 0.01$ M, the phosphorylation of the KSP repeats in the H and M tails leads to a major transformation of the NF brush structure. When almost half of all KSP repeats are phosphorylated ($v_c \approx -1$), the longest tails (H)
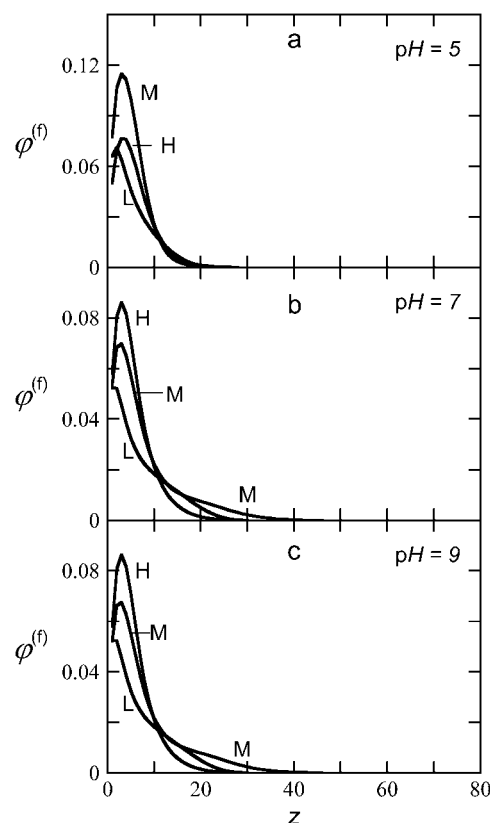
FIGURE 5 The overall volume fraction profiles of the L, M, and H chains at the physiological relevant ionic strength of $c_s = 0.15$ M salt, for (a) pH = 5, (b) pH = 7, and (c) pH = 9. Other parameters as in Fig. 3.

undergo a sharp conformational transition, relocating the terminal part from near the NF backbone to the periphery of NF brush. To quantify this phenomenon, we consider the average z-position h_g of the terminal monomer (free end) for each of the tails (H, M, and L) as a function of the effective valency v_c (or, equivalently, of the acquired charge $\Delta Q = v_c N_{KSP}$). For each type of the tail (H, M, or L), the average position h_g of the tail end-point is calculated as

$$h_g = \frac{\int zg(z)L(z)dz}{\int g(z)L(z)dz} = \int zg(z)L(z)l dz, \qquad (1)$$

where $g(z)$ is the volume fraction of the free ends at distance z from the backbone, $L(z)$ is the number of sites in the cylindrical layer, $L(z) \sim (R/a + z)$, and l is the average distance between the tails. Due to the normalization in Eq. 1, we can interpret h_g as a direct measure of the tail extension.

A selection of the data for the average end-point positions h_g for the three H, M, and L tails is presented in Fig. 6. Here we show how these end-point positions respond to changes in the effective charge v_c and how this is affected by the ionic strength of the solution in the range from $c_s = 0.001$ M (a), to 1 M (d). The dependence of h_g on v_c is shown in Fig. 6, a–c, from which it is found that, up to $c_s = 0.1$ M, the general trends are similar. In a dephosphorylated state ($v_c = 0$) the average positions of the free ends of the tails demonstrate the trends found for the overall polymer volume fraction profiles φ. Namely, the intermediate (M) tails are extended the most and their free ends are located at the brush periphery. The shortest tails (L) fill the proximal region, whereas the longest tails (H) are found near the NF backbone. The increase in the effective charge v_c leads to a gradual monotonic increase in h_g for the M tail, a cooperative relocation of the H tail to the

periphery of the brush (h_g stays almost unaffected up to $v_c \approx -1$ and then rapidly increases, particularly at lower ionic strength), and a nonmonotonic variation in h_g for the L tail. The initial increase in h_g for the L tail (which has no KSP repeats and, thereby, is not directly involved in the phosphorylation process) is caused by the ionization of the KSP repeats in the H and M tails and the increased electrostatic repulsion between similarly charged tails. When, however, the H tails start to relocate to the NF brush periphery, the extension of the L tails decreases, and the average position h_g of the L tail stays virtually constant upon further phosphorylation of the neurofilament.

The pH dependence of the height h_g for the triplet H, M, and L chains is presented in Fig. 8 for three levels of phosphorylation at physiological ionic strength conditions $c_s = 0.15$ M. The NF brush is essentially insensitive to the pH for the regime pH > 6 (unless pH > 10). The trends of the height for the basic regime and how these change with phosphorylation have been shown in Fig. 6 and need no further discussion. In the acidic regime the chains become positively charged, and depending on the level of phosphorylation, the height of the H and M chains go through a pronounced minimum. Below pH = 5 we find a strong height dependence on the pH. The increase in height with decreasing pH is shifted to lower pH when the chains are more strongly phosphorylated. The reason is that the iso-electric point shifts to lower pH values when the phosphorylation goes up. Interestingly, the end-point of the L chain goes through a (small) maximum around pH = 5 when the M and H chains are phosphorylated. This maximum occurs when the other two chains have their minimum extension. The shortest L chains then can extend further than the longer ones.
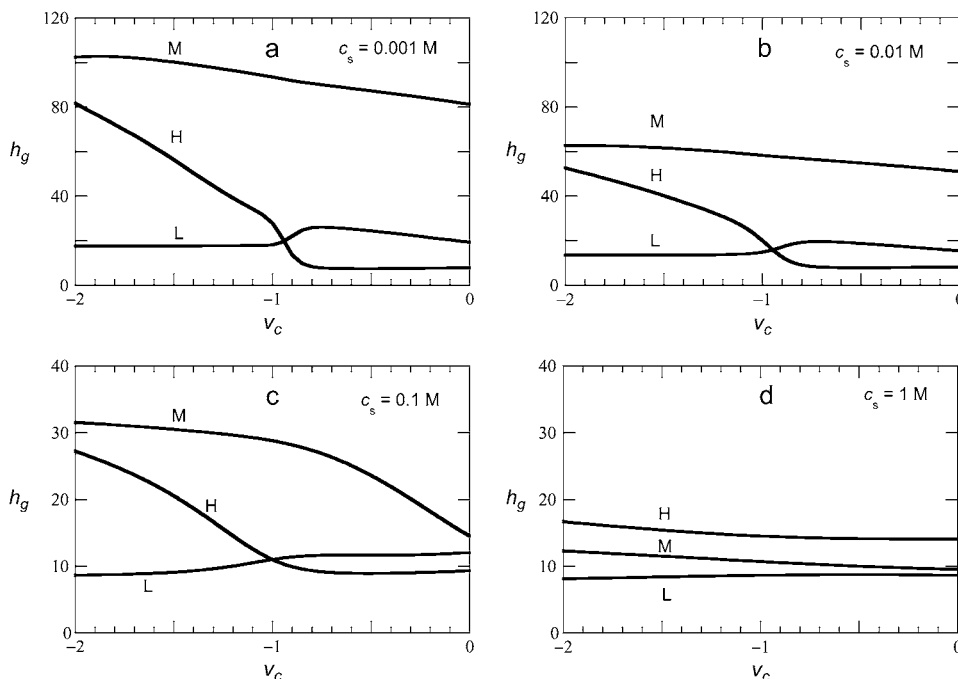
FIGURE 6 The average position h_g of end monomers for the H, M, and L tails as a function of the effective valency v_c of the serines in the KSP repeats due to (partial) phosphorylation, at a fixed pH = 7 and for a wide range of ionic strength conditions. (a) $c_s = 0.001$ M, (b) $c_s = 0.01$ M, (c) $c_s = 0.1$ M, and (d) $c_s = 1$ M.
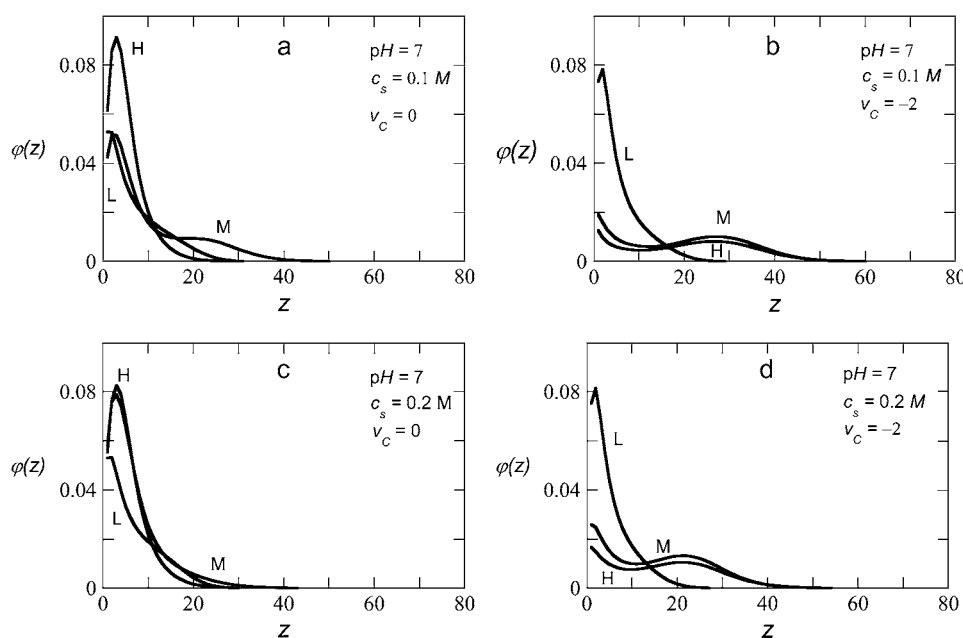
FIGURE 7 Volume fraction profiles of L, M, and H tails under physiologically relevant conditions: pH = 7; ionic strength is $c_s = 0.1$ M (*a* and *b*); $c_s = 0.2$ M (*c* and *d*); without phosphorylation $v_C = 0$ (*a* and *c*); and at fully phosphorylated state $v_c = -2$ (*b* and *d*).

Additional insights in the NF brush phosphorylation under the conditions close to physiological (pH $\approx$ 7, $c_s \approx 0.15$ M) can be obtained from the polymer density profiles $\varphi(z)$ in Fig. 7. The SCF data presented in Fig. 7 allows for comparison between polymer density distributions in dephosphorylated ($v_c = 0$) and fully phosphorylated ($v_c = -2$) states of the NF brush for the values of $c_s = 0.1$ M (Fig. 7, *a* and *b*) and $c_s = 0.2$ M (Fig. 7, *c* and *d*), just below and just above the physiological ionic strength of $c_s \approx 0.15$ M . (Fig. 7 *a* was already discussed earlier as part of Fig. 3, and we reproduce it here for convenience.) Comparison of Fig. 7, *a* and *c*, reveals qualitative changes in the NF brush structure due to a twofold increase in the ionic strength. Whereas the volume fraction profiles for the H and L tails stay almost unchanged, the bimodal distribution of the M tails (noticeably shifted to the brush periphery at $c_s = 0.1$ M) becomes unimodal and approaches that of the H tails at $c_s = 0.2$ M. The phosphorylation of the M and H tails leads, however, to a qualitatively similar picture (Fig. 7, *b* and *d*). The polymer volume fraction profiles of the M and H tails become almost identical with a cutoff at $z/a \approx 45$. The values of polymer volume fraction cutoff in Fig. 7 provide upper limit estimates for the physiologically relevant NF brush thickness of $\sim 35a \approx 21$ nm and $45a \approx 27$ nm in a dephosphorylated ($v_c = 0$) and a fully phosphorylated ($v_c = -2$) state, respectively. In an axon, the interneurofilament spacing is expected to be approximately twofold larger than the thickness of an individual NF due to cross-bridging between terminal KEP domains. Therefore, the mean spacing should stay below 42 and 54 nm in a dephosphorylated and fully phosphorylated states of the NF brush, respectively. These estimates are in good agreement with the interneurofilament distances in axons of mouse optic nerves, measured at two different

positions 50 and 700 μm from the eye (21). The measured distributions of interneurofilament spacing in adult mouse were rather wide with distinct maxima at $\sim$30 and 40 nm for the 50- and 700-μm positions, respectively. The increase in characteristic interfilament spacing with distance along the optic axon correlates with earlier findings (22,23) that NFs within the perikaryon and proximal segments of neurites are hypophosphorylated, while NFs in distal parts of axons are heavily phosphorylated. We note that no adjustable parameters were used in the SCF calculations and the values of chosen parameters $a = 0.6$ nm and $\chi = 0-2$ are typical for flexible polymers in various solvents.

A further increase in the ionic strength to $c_s > 0.2$ M affects mostly the structure of a phosphorylated NF. The NF brush shrinks, but the general trend to expel the M and H tails to the outside is retained up to the solution salinity $c_s \lesssim 1$ M. When the ionic strength is high ($c_s = 1$ M, Fig. 6 *d*) and the electrostatic interactions are almost fully screened, the phosphorylation of the NF brush affects the conformations of the tails and average positions of end monomers rather weakly. In a dephosphorylated state ($v_c = 0$) the polymer volume fraction distribution (Fig. 3 *c*) is close to that in Fig. 7 *c*, and the free ends of the longest tails (H) are spread throughout the brush (Fig. 4 *c*). The cooperative relocation of the H tail (predicted at lower ionic strength) is now substituted by a weak gradual increase in h_g. The average end-point position of the M tail also increases, whereas the L tail exhibits a minor decrease in h_g.

Collapse-to-stretching transition of the H tails

We now focus on the signatures of the cooperative relocation of the H tails in more detail. Fig. 6, *a–c*, clearly indicate that

the h_g versus v_c dependences for the H tails exhibit three distinct regimes. When $-1 \lesssim v_c < 0$, the average end position h_g is almost independent of v_c and of the ionic strength in the solution c_s. In the vicinity of $v_c \approx -1$, the average end-point position h_g starts to increase. This range of v_c corresponds to the disproportionation of the H tails (part of them is still localized near the NF backbone, whereas the remainder have already relocated to the brush periphery). Here, the slope $\partial h_g / \partial v_c$ noticeably increases with a decrease in the ionic strength c_s. Interestingly, the location of the transition regime ($v_c \simeq -1$) is virtually independent of c_s (in the range of $c_s \lesssim 0.1$ M). A comparison of Fig. 6, *a–c*, indicates that the transition value of v_c (specified as an intersection point of h_g for the H and L tails) is the same for $c_s = 0.001$ M and $c_s = 0.01$ M ($v_c \approx -0.95$), and is only slightly shifted for $c_s = 0.1$ M ($v_c \approx -1.0$). Finally, when $-2 < v_c \lesssim -1$, the average end-point position h_g increases according to a different law.

The response of the H tails upon the phosphorylation can be rationalized on the basis of an analytical model developed in the Appendix. In this framework the H tails are envisioned as a polyelectrolyte cylindrical brush under poor solvent conditions. The free ends are fixed at the outer boundary of the brush, and all the components (the aa units along the chain and salt ions) are smeared uniformly throughout the brush. We briefly summarize here the predictions of this analytical model and refer to the Appendix for more detail.

The electrostatic repulsion between the tethered chains with fraction α of charged monomers (corresponding to the partially phosphorylated H tails with $v_c < 0$) and the attractive nonelectrostatic interactions with a negative second virial coefficient $-\tau a^3$ (corresponding to the hydrophobic attraction between apolar aa residues) compete with each other. At high ionic strength (in the so-called salt-dominated regime when the concentration of ions c_s greatly exceeds the concentration of the intrinsic brush charge c_{charge}), the electrostatic repulsion gives rise to an effective second virial coefficient v_{el} for the monomer-monomer interactions, $v_{el}a^3 \simeq \alpha^2/c_s$. The ionization-induced swelling of the brush is gradual in this regime (as in Fig. 6 *d*).

At low ionic strength, the ionization of the brush leads to an abrupt (jumpwise) increase in the overall brush thickness at $\alpha = \alpha^{tr}$. Such a scenario is possible only when the ionic strength in the solution becomes smaller than a certain critical value, $c_s < c_s^{cr}$ (Eq. 18 in the Appendix). The degree of ionization α^{tr} is, in scaling terms, independent of the salt concentration c_s (Eq. 17). Below the transition point $\alpha < \alpha^{tr}$, the brush is collapsed. Its thickness is independent of c_s or α (Eq. 13) and is solely determined by the value of τ (the strength of the attractive monomer-monomer contacts). Above the transition point $\alpha > \alpha^{tr}$, the tethered chains are stretched due to the difference in ion osmotic pressure inside and outside the brush, and the brush thickness continues to increase ($\sim \alpha^{1/2}$) upon a further increase in α (Eqs. 14 and 16). The scaling for the brush thickness with the ionic strength ($\sim c_s^{-1/4}$) is expected in the salt-dominated regime for the
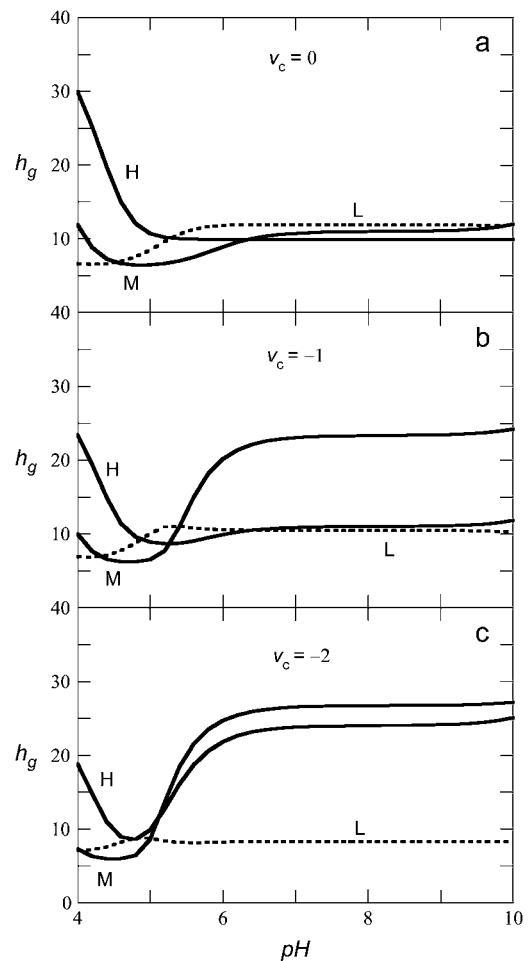

FIGURE 8 The average position h_g of the end monomers of the H, M, and L tails as a function of the pH for three values of the phosphorylation of the KSP repeats at fixed value of the ionic strength $c_s = 0.15$ M. (*a*) $v_c = 0$, (*b*) $v_c = -1$, and (*c*) $v_c = -2$.

stretched brush (Eq. 16). The predicted power laws are asymptotic (i.e., valid in the limit of long chains $N \gg 1$ and dense grafting), and all the numerical coefficients are omitted.

Fig. 9 collects the relevant SCF data for $h_g(v_c)$ for the H tails at various ionic strength conditions. Although the predictions of the analytical model cannot blindly be transferred to the H tails in the NF brush (the latter are multicomponent ampholytic polymers that have a specified position of each ionizable KSP repeat sequence and each hydrophobic aa residue along the chain), Figs. 6 and 9 point to striking similarities between the SCF results and the analytical framework.

1. At relatively low ionic strengths the relocation of the H tails to the brush periphery (initially noticeable by the increase in h_g) occurs at a degree of phosphorylation $v_c \approx -1$, irrespective of the solution salinity (when $c_s \lesssim 0.1$ M). At a higher ionic strength ($c_s = 1$ M) the variation of h_g with the effective charge v_c is smooth and gradual.
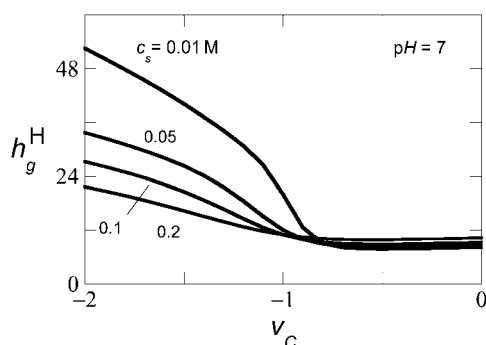
FIGURE 9 The average end-point distribution of the H tails as a function of the charge v_C (in units of the elementary charge). pH = 7 and the ionic strength is indicated.

2. A jumpwise increase in the brush thickness, predicted by the analytical model, is traced to a strong gradient for $h_g(v_c)$ in the transition region ($v_c \approx -1$) upon a decrease in the ionic strength. The predicted jumpwise variation in brush thickness is the direct consequence of the underlying approximation that all the free ends are fixed at the brush external boundary. The SCF approach relaxes this constraint (Fig. 4 indicates that the terminal monomers of the tails have a wide distribution), and the relocation of the H tails occurs as a cooperative, but continuous transition. The width of this transition (associated with the slope $\partial v_c/\partial h_g$) decreases with decreasing ionic strength, thus indicating the increase in the transition cooperativity.
3. In the pretransition interval for the degrees of phosphorylation given by $-1 \lesssim v_c < 0$, all the SCF data in Fig. 9 collapse to the same number $h_g \approx 9a$, irrespective of the values of v_c and c_s in the whole range of $c_s \lesssim 0.1$ M.
4. In the post-transition interval, that is for $-2 < v_c \lesssim -1$, both, an increase in v_c and a decrease in c_s leads to a noticeable increase in the brush thickness h_g. This is in agreement with the analytical predictions. However, a closer inspection of the $h_g(v_c)$ and $h_g(c_s)$ dependences for the H tails in the post-transition regime, indicates larger values of apparent exponents than predicted by the analytical model. For example, exponent γ (specified as $h_g \sim v_c^\gamma$) is estimated from the SCF calculations as $\gamma \gtrsim 1$, whereas the analytical prediction is $\gamma = 0.5$ (see the Appendix). We note that in the analytical framework all the chains are of only one type. In contrast, in the NF brush the H tails interact also with the sublayer of L-tails (and intermediate M-tails). The electrostatic repulsive force between a phosphorylated H and an L tail (the latter is not directly involved in the phosphorylation process) is proportional to the acquired charge $\Delta Q_H \sim v_c$. As a result, the elastic stretching of the H tail is expected to increase $\sim v_c$ to provide $\gamma = 1$, strictly due to the H-L interaction. Therefore, the discrepancy between the SCF and analytical exponents (value of $\gamma > 1$) can be attributed to the additional H-L and H-M interactions in the NF brush.

Summarizing, we find that the SCF data for the phosphorylation-induced relocation of the H tails is in reasonable agreement with the trends predicted by a simple box-like analytical model for a cylindrical polyelectrolyte brush in a poor solvent.

CONCLUSIONS

The numerical self-consistent field and an analytical frameworks were applied to investigate the equilibrium structure of the human neurofilament brush in different environments including those with close to normal physiological conditions. The modeling was performed both with a simple (copolymer type) and a more refined coarse-graining of the actual aa sequences in the projection domains of the NF proteins. Both models reveal an inhomogeneous structure of the NF brush up to physiological conditions. Different solubilities of the aa residues in water were accounted for in fine model f, which predicts a higher local concentration of the aa residues near the backbone of the NF. At higher solution salinity, where the electrostatic interactions are strongly screened, the on average large values of the Flory parameter χ (that determine the hydrophobicity of the aa residues in our SCF modeling) become increasingly important in specifying the NF brush structure.

The ionization of the KSP repeats in the NF-H and NF-M side arms leads to the increase in the NF brush size and triggers a major relocation of the H tails from the NF backbone to the periphery of the brush. The transition takes place when almost 50% of all KSP repeats are phosphorylated. This prediction holds in the full range of ionic strength $c_s \lesssim 0.1$ M and can be rationalized within an analytical framework (developed in the Appendix). The phosphorylation of the KSP repeats in the central part of the H tail does not perturb its terminal cross-bridging (KEP) domain that translocates to the NF brush periphery and becomes more available for cross-bridging. Based on this observation we argue that for the ionic strength range $c_s \lesssim 0.1-0.2$ M, the moderate phosphorylation increases the propensity of the H tails to cross bridge.

At high solution salinity ($c_s \simeq 1$ M) the equilibrium structure of a dephosphorylated NF brush is essentially homogeneous. The polymer volume fraction profiles for all the H, M, and L tails, become almost similar. The corresponding distributions of the free ends are of bell-like shape with slight predominance of intermediate M tails at the brush periphery. Moderate phosphorylation of such an NF leads to minor changes in the brush structure (polymer volume fraction profiles for the H and M tails become more extended and less steep) where it leads just to a slight increase in the average height of the H and M tails.

The screening of the electrostatic interactions suggests that under physiological conditions in axons, the phosphorylation-induced processes in the cytoskeletonal NFs occur independently. Based on this assumption and the SCF data for an

individual NF, we argue that a moderate phosphorylation of the triplet proteins may lead to an increase in the interfilament distance in axons with a simultaneous stabilization of the NF network. The latter prediction implies that the fraction of cross bridges is expected to increase upon an increase in the phosphorylation level provided that no other axonal processes interfere. This prediction could possibly be probed experimentally if the number of cross bridges in different cross-sections along the axons could be quantified in the same way as done for the interneurofilament spacing in the mouse optic nerve (21).

Our conclusions summarize the results of one-dimensional SCF modeling for the case when only the serines in KSP repeats were phosphorylated. An interesting extension of this study would be to explore how hyperphosphorylation involving the serines (and threonines) elsewhere in the projection domains would affect the NF brush structure and the propensity of the H tails to cross bridge.

APPENDIX: COLLAPSE-TO-STRETCHING TRANSITION IN A CYLINDRICAL POLYELECTROLYTE BRUSH

We use the Alexander-de Gennes boxlike model (24) to analyze the behavior of a cylindrical polyelectrolyte brush under poor solvent conditions. This model has successfully been applied before to describe a planar polyelectrolyte brush in various solvents (25–28).

We consider a brush of negatively charged polyelectrolyte chains of thickness D, tethered to a cylinder of radius $R \ll D$. The distance between the chains along the axis of cylinder is $l < a\sqrt{N}$, where $N \gg 1$ is number of monomers per chain, and a is monomer size. The brush is immersed in solution of monovalent salt of concentration c_s, and α is the fraction of ionized monomers ($\alpha = Q/N$ where Qe is the total chain charge). The Debye screening length in the solution is $r_D = 1/\sqrt{8\pi l_B c_s}$, where $l_B = e^2/\epsilon k_B T \simeq a$ is the Bjerrum length (ϵ is the dielectric constant, k_B is the Boltzmann constant, and T is temperature). The polymer is uniformly spread within the brush and its volume fraction is given by $\varphi = Na^3/\pi h l D^2 \ll 1$. The corresponding charge concentration is $c_{charge} = \alpha N/\pi l D^2 = \alpha \varphi a^{-3}$.

The solvent quality is specified by the second virial coefficient of monomer-monomer interactions νa^3. In a θ-solvent $\nu = 0$, and the monomer-monomer interactions are governed by ternary contacts with the third virial coefficient $wa^6 \simeq a^6$. In a poor solvent, ν is determined by the relative deviation $\tau = (\theta - T)/T$ from the θ-temperature as $\nu \simeq -\tau < 0$. Below we focus on the case of relatively dense brush, $a/l > \tau$. (Under these conditions a collapsed cylindrical brush remains laterally homogeneous (29).)

The free energy ΔF per chain in the brush comprises a contribution due to the attractive binary contacts between monomers (first term in Eq. 2), a term due to the repulsive ternary contacts (second term in Eq. 2, one due to the elastic stretching of the chains (third term in Eq. 2) and finally an electrostatic free energy ΔF_{el},

$$\frac{\Delta F}{k_B T} \simeq -N\tau\varphi + N\varphi^2 + \frac{D^2}{a^2 N} + \frac{\Delta F_{el}}{k_B T}. \quad (2)$$

Here and below, the numerical coefficients on the order of unity are omitted.

The electrostatic contribution ΔF_{el} is calculated as explained in Halperin et al. (28) with an account of the system cylindrical symmetry. We introduce a compensation length $\lambda > H$, beyond which the brush charge is totally screened. At distances smaller than λ, the distribution of monovalent ions is perturbed. The cylindrical layer of thickness λ contains n_+ and n_- uniformly spread salt ions per unit length of the cylinder,

$$n_+ = n_- + \frac{\alpha N}{l} = n_- + q, \quad (3)$$

where $q = \alpha N/l$ is the brush charge per unit length of the cylinder. The charge compensation (Eq. 3) implies $c_+ = c_- + q/\pi\lambda^2$, where $c_\pm = n_\pm/\pi\lambda^2$ are the respective concentrations of ions in a layer with thickness λ. An additional relationship between c_+ and c_- follows from equality of ion chemical potentials in the brush and in the bulk solution (the Donnan rule), $c_+ c_- = c_s^2$. The c_+ and c_- concentrations are therefore interrelated as

$$\frac{c_\pm}{c_s} = \pm \frac{4q l_B r_D^2}{\lambda^2} + \sqrt{1 + \frac{16q^2 l_B^2 r_D^4}{\lambda^4}}. \quad (4)$$

The translational entropy of ions ΔS_u per unit length of the cylinder yields

$$-\frac{\Delta S_u}{k_B} = n_+ \ln\left(\frac{c_+}{c_s}\right) + n_- \ln\left(\frac{c_-}{c_s}\right)$$
$$= q \ln\left(\frac{4q l_B r_D^2}{\lambda^2} + \sqrt{1 + \frac{16q^2 l_B^2 r_D^4}{\lambda^4}}\right). \quad (5)$$

The electrostatic energy per unit length of the cylinder $\Delta W_u = \epsilon/4 \int_0^\lambda E(r)^2 r dr$ is calculated by using the Gauss theorem for the electric field $E(r)$, $E(r) = 2Q_u(r)/r\epsilon$, where $Q_u(r)$ is the charge per unit length within the cylindrical layer of radius r,

$$Q_u(r) = q \begin{cases} r^2/D^2 - r^2/\lambda^2 & 0 < r < D \\ 1 - r^2/\lambda^2 & D < r < \lambda \end{cases}. \quad (6)$$

The result is

$$\frac{\Delta W_u}{k_B T} = \frac{l_B q^2}{2}\left[\ln\left(\frac{\lambda^2}{D^2}\right) - 1 + \frac{D^2}{\lambda^2}\right]. \quad (7)$$

The total free energy $\Delta F_u = \Delta W_u - T\Delta S_u$ per unit length of the cylinder yields

$$\frac{\Delta F_u}{k_B T} = \frac{l_B q^2}{2}\left[\ln\left(\frac{\lambda^2}{D^2}\right) - 1 + \frac{D^2}{\lambda^2}\right]$$
$$+ q \ln\left(\frac{4q l_B r_D^2}{\lambda^2} + \sqrt{1 + \frac{16q^2 l_B^2 r_D^4}{\lambda^4}}\right). \quad (8)$$

The minimization of ΔF_u with respect to λ for a given value of D, $\partial \Delta F_u/\partial \lambda = 0$, provides an equation that relates the compensation length λ to the brush thickness D and the Debye radius r_D,

$$(\lambda^2 - D^2)\sqrt{1 + \frac{16q^2 l_B^2 r_D^4}{\lambda^4}} = 8r_D^2. \quad (9)$$

The analysis of Eq. 9 allows for a scaling type representation of $\lambda = \lambda(D, q l_B, r_D)$ dependences.

The electrostatic brush regimes

When the ionic strength in solution is low, $r_D \gg D$, and the brush is weakly charged, $q l_B \ll 1$, the electrostatic interactions in the brush are essentially unscreened ($c_{charge} \gg c_+, c_-$). Here, the compensation length $\lambda \simeq r_D \gg D$, and the free energy ΔF_u is dominated by the electrostatic energy ΔW_u. This regime is referred to as the ''charged regime''. The free energy per chain $\Delta F_{el} = \Delta F_u l$ is specified here as

$$\frac{\Delta F_{\text{el,charged}}(D)}{k_B T} \simeq q^2 l_B l \ln\left(\frac{r_D^2}{D^2}\right). \qquad (10)$$

When the brush is strongly charged, $q l_B \gg 1$, the counterions are retained in the brush to compensate the brush charge, $c_{\text{charge}} \approx c_+ \gg c_-$. Here, the compensation length $\lambda \simeq D(1+\delta_o)$, and $\delta_o \simeq 1/q l_B \ll 1$. The free energy ΔF_u is dominated by the ion entropy ΔS_u, and this regime is referred to as the osmotic regime. In the osmotic regime the electrostatic free energy per chain is given by

$$\frac{\Delta F_{\text{el,osm}}(D)}{k_B T} \simeq q l \ln\left(\frac{q l_B r_D^2}{D^2}\right). \qquad (11)$$

An increase of the ionic strength levels the ion concentrations between inside and outside, that is $c_+ \gtrsim c_- \approx c_s$. At larger ionic strength $c_s \gg c_{\text{charge}}$, the brush is found in the so-called salt-dominated regime. Here, the compensation length $\lambda \simeq D(1+\delta_s)$ and $\delta_s \simeq r_D^2/D^2 \ll 1$. Here, ΔF_u is determined by the ion entropy ΔS_u, and the electrostatic free energy per chain $\Delta F_{\text{el}} = \Delta F_u l$ is given by

$$\frac{\Delta F_{\text{el,salt}}(D)}{k_B T} \simeq q^2 l_B l \left(\frac{r_D^2}{D^2}\right) \simeq N \varphi v_{\text{el}}, \qquad (12)$$

where $v_{\text{el}} a^3 \simeq \alpha^2 l_B r_D^2 \simeq \alpha^2/c_s$ is the electrostatic second virial coefficient for the monomer-monomer interactions.

The collapse-to-stretching transition

At low charge density along the chains (weak ionization) the tethered chains are collapsed (the first two terms in Eq. 2 dominate). The balance between the attractive binary and repulsive ternary interactions gives

$$D_{\text{glob}} \simeq a\sqrt{\frac{Na}{\tau l}}; \quad \frac{\Delta F_{\text{glob}}}{k_B T} \simeq -N\tau^2 + \frac{\Delta F_{\text{el}}(D_{\text{glob}})}{k_B T}. \qquad (13)$$

In strongly charged brushes, the third and fourth terms in Eq. 2 dominate, and the balance of the elastic and the electrostatic contributions (Eqs. 10–12) determine the brush thickness D and the free energy per chain ΔF in all three regimes (osmotic, charged, and salt-dominated),

$$D_{\text{osm}} \simeq a\alpha^{1/2}N; \quad \frac{\Delta F_{\text{osm}}}{k_B T} \simeq \alpha N \ln\left(\frac{\alpha N l_B r_D^2}{l D_{\text{osm}}^2}\right), \qquad (14)$$

$$D_{\text{charged}} \simeq a\alpha\left(\frac{l_B}{l}\right)^{1/2}N^{3/2}; \quad \frac{\Delta F_{\text{charged}}}{k_B T} \simeq \frac{\alpha^2 N^2 l_B}{l}\ln\left(\frac{r_D^2}{D_{\text{charged}}^2}\right), \qquad (15)$$

$$D_{\text{salt}} \simeq \left(\alpha^2 r_D^2 a^2\right)^{1/4}\left(\frac{l_B}{l}\right)^{1/2}N^{3/4};$$

$$\frac{\Delta F_{\text{salt}}}{k_B T} \simeq N v_{\text{el}}\varphi \simeq \frac{\alpha^2 N^2 l_B}{l}\left(\frac{r_D^2}{D_{\text{salt}}^2}\right). \qquad (16)$$

Equations 13–16 allow us to obtain the degree of brush ionization α^{tr} that corresponds to the jumpwise increase in brush thickness. By equating the free energies in the collapsed and the stretched states of the brush, we find (with the accuracy of the logarithmic corrections),

$$\alpha^{\text{tr}} \simeq \begin{cases} \tau^2 & l/l_B \ll N\tau^2 \\ \tau\sqrt{l/aN} & l/l_B \gg N\tau^2 \end{cases}, \qquad (17)$$

where the first and the second lines in Eq. 17 correspond to the osmotic and the charged states of the collapsed brush, respectively.

The jumpwise character of the collapse-to-stretching transition is retained up to a certain critical value of the solution salinity ($r_D > r_D^{\text{cr}}$),

$$r_D^{\text{cr}} \simeq \begin{cases} a/(\tau^{3/2}) & l/l_B \ll N\tau^2 \\ a\sqrt{Na/l\tau} & l/l_B \gg N\tau^2 \end{cases}. \qquad (18)$$

The scaling expressions for r_D^{cr} follow from the two requirements:

1. The collapsed state must be at the boundary between the salt-dominated and either the osmotic or the charged states (the first and the second lines in Eq. 18, respectively), and
2. $v_{\text{el}} \approx \tau$ (the onset of the effective θ-conditions).

The increase in brush thickness becomes gradual when $r_D < r_D^{\text{cr}}$. This growth in thickness is governed by an effective second virial coefficient $v_{\text{eff}} = -\tau + v_{\text{el}} \simeq -\tau + \alpha^2 r_D^2 l_B^2$ (26).

We note that the absence of a power law dependence of α^{tr} on r_D (or, $c_s \sim r_D^{-2}$) is a result of the brush cylindrical symmetry. In a planar brush, a power law dependence for α^{tr} on c_s was predicted at sparse grafting of the chains (27).

REFERENCES

1. Caims, N. J., V. M.-Y. Lee, and J. Q. Trojanowski. 2004. The cytoskeleton in neurodegenerative diseases. *J. Pathol.* 204:438–449.

2. Julien, J. P. 1999. Neurofilament functions in health and disease. *Curr. Opin. Neurobiol.* 9:554–560.

3. Hoffman, P. N., D. W. Cleveland, J. W. Griffin, P. W. Landers, N. J. Cowan, and D. L. Price. 1987. Neurofilament gene expression: a major determinant of axonal caliber. *Proc. Natl. Acad. Sci. USA.* 84:3472–3476.

4. Chou, Y.-H., and R. D. Goldman. 2000. Intermediate filaments on the move. *J. Cell Biol.* 150:F101–F105.

5. Janmey, P. A., J.-F. Leterrier, and H. Herrmann. 2003. Assembly and structure of neurofilaments. *Curr. Opin. Colloid Int. Sci.* 8:40–47.

6. Yuan, A., M. V. Rao, T. Sasaki, Y. Chen, A. Kumar, Veeranna, R. K. H. Liem, J. Eyer, A. C. Peterson, J. P. Julien, and R. A. Nixon. 2006. α-Internexin is structurally associated with the neurofilament triplet proteins in the mature CNS. *J. Neurosci.* 26:10006–10019.

7. Hisanaga, S.-I., A. Ikai, and N. Hirokawa. 1990. Molecular architecture of the neurofilament. I. Subunit arrangement of neurofilament L protein in the intermediate-sized filament. *J. Mol. Biol.* 211:857–869.

8. Hisanaga, S.-I., and N. Hirokawa. 1990. Molecular architecture of the neurofilament. II. Reassembly process of neurofilament L protein in vitro. *J. Mol. Biol.* 211:871–882.

9. Mukhopadhyay, R., S. Kumar, and J. H. Hoh. 2004. Molecular mechanisms for organizing the neuronal cytoskeleton. *Bioessays.* 26:1–9.

10. Kumar, S., X. Yin, B. D. Trapp, J. H. Hoh, and M. E. Paulatis. 2002. Relating interactions between neurofilaments to the structure of axonal neurofilament distribution through polymer brush models. *Biophys. J.* 82:2360–2372.

11. Brown, H. G., and J. H. Hoh. 1977. Entropic exclusion of neurofilament side arms: a mechanism for maintaining interfilament spacing. *Biochemistry.* 36:15035–15040.

12. Hoh, J. H. 1998. Functional protein domains from the thermally driven motion of polypeptide chains: a proposal. *Proteins Struct. Funct. Genet.* 32:223–228.

13. Mukhopadhyay, R., and J. H. Hoh. 2001. AFM force measurements on microtubule-associated proteins: the projection domain exerts a long-range repulsive force. *FEBS Lett.* 505:374–382.

14. Zhulina, E. B., and F. A. M. Leermakers. 2007. A self-consistent field analysis of the neurofilament brush with amino-acid resolution. *Biophys. J.* 93:1421–1430.

15. Leermakers, F. A. M., P. J. Atkinson, E. Dickinson, and D. S. Horne. 1996. Self-consistent field modeling of adsorbed β-casein: effects of pH and ionic strength on surface converge and density profile. *J. Colloid Int. Sci.* 178:681–693.

16. Claessens, M. M. A. E., B. F. van Oort, F. A. M. Leermakers, F. A. Hoekstra, and M. A. Cohen Stuart. 2004. Charged lipid vesicles: effects of salts on bending rigidity, stability, and size. *Biophys. J.* 87:3882–3893.

17. Kik, R. A., F. A. M. Leermakers, and J. M. Kleijn. 2005. Molecular modeling of lipid bilayers and the effect of protein-like inclusions. *Phys. Chem. Chem. Phys.* 7:1996–2005.

18. Hirokawa, N. 1982. Cross-linker system between neurofilaments, microtubules and membranous organelles in frog axons revealed by the quick-freeze, deep-etching method. *J. Cell Biol.* 94:129–142.

19. Chen, J. G., T. Nakata, Z. Z. Zhang, and N. Hirokawa. 2000. The C-terminal tail domain of neurofilament protein −H (NF-H) forms the cross bridges and regulates neurofilament bundle formation. *J. Cell Sci.* 113:3861–3869.

20. Fleer, G. J., M. A. Cohen-Stuart, J. M. H. M. Scheutjens, T. Cosgrove, and B. Vincent. 1993. Polymers at Interfaces. Chapman & Hill, London.

21. Sanchez, I., L. Hassinger, R. K. Sihag, D. W. Cleveland, P. Mohan, and R. A. Nixon. 2000. Local control of neurofilament accumulation during radial growth of myelinating axons in vivo: selective role of site-specific phosphorylation. *J. Cell Biol.* 151:1013–1024.

22. Lee, V. M.-Y., M. J. Carden, W. W. Schlaepfer, and J. Q. Trojanowski. 1987. Monoclonal antibodies distinguish several differentially phosphorylated states of the two largest rat neurofilament subunits (NF-H and NF-M) and demonstrate their existence in the normal nervous system of adult rats. *J. Neurosci.* 7:3478–3488.

23. Carden, M. J., J. Q. Trojanowski, W. W. Schlaepfer, and V. M.-Y. Lee. 1987. Two-stage expression of neurofilament polypeptides during rat neurogenesis with early establishment of adult phosphorylation patterns. *J. Neurosci.* 7:3499–3504.

24. Alexander, S. 1977. Adsorption of chain molecules with a polar head—a scaling description. *J. Phys. (Paris).* 38:983–987.

25. Pincus, P. 1991. Colloid stabilization with grafted polyelectrolytes. *Macromolecules.* 24:2912−2919.

26. Borisov, O. V., T. M. Birshtein, and E. B. Zhulina. 1991. Collapse of grafted polyelectrolyte layer. *J. Phys. II.* 1:521–526.

27. De Kruif, C. G., and E. B. Zhulina. 1996. Kappa-casein as a polyelectrolyte brush on the surface of casein micelles. *Colloid Surf. A.* 117:151–159.

28. Halperin, A., A. Buhot, and E. B. Zhulina. 2004. Sensitivity, specificity and hybridization isotherms of DNA chips. *Biophys. J.* 86:718–730.

29. Sheiko, S. S., O. V. Borisov, S. A. Prokhorova, and M. Möller. 2004. Cylindrical molecular brushes under poor solvent conditions: microscopic observation and scaling analysis. *Eur. Phys. J. E.* 13:125–131.